fractal and fractional

MDPI

Article

Study on the Mechanical Properties and Microstructural Fractal Characteristics of Ternary Red-Mud-Based Cementitious Materials

Hu Huang [1,*], Yongsheng Zhang [1], Ruihang Li [1], Qingming Qiu [2] and Changbo Song [3]

[1] School of Water Conservancy, North China University of Water Resources and Electric Power, Zhengzhou 450046, China; 18239200860@163.com (Y.Z.); x20231010030@stu.ncwu.edu.cn (R.L.)
[2] School of Civil Engineering, Tianjin University, Tianjin 300072, China; lemoncc_717@tju.edu.cn
[3] Power China Beijing Engineering Corporation Limited, Beijing 100024, China; songchangbo@bjy.powerchina.cn
* Correspondence: huanghu@ncwu.edu.cn

Abstract

Red mud (RM), a waste residue from alumina extraction, poses serious environmental impacts on water resources, land resources, and ecological systems due to its large production, high alkalinity, and low resource utilization. To enhance the overall utilization rate of RM solid-waste materials, this study focuses on RM, blast furnace slag (BFS), and fly ash (FA) cementitious materials as the research objects. Through mechanical tests and microstructural analysis, the optimal mix ratio of the ternary RM-based cementitious material is determined, and a systematic study of its microstructural evolution is conducted. Concurrently, fractal theory was used to quantify the microstructure of the material, revealing the evolution laws of the mechanical properties of ternary red-mud-based cementitious materials from a mesoscopic perspective. The results indicate that reducing the proportion of RM or slag alone to increase the FA content yields inferior modification effects compared to simultaneously reducing the proportions of both RM and BFS to increase FA content. Compared with the binary RM-based cementitious material made of RM and BFS, the 28-day compressive strength increases by approximately 25%, reaching 50 MPa. The incorporation of FA can reduce the volume of harmful pores in the cementitious matrix, providing ample reactive material for subsequent hydration reactions, promoting later hydration products, and improving the distribution of the internal pore structure. This leads to increases in both fractal dimensions, and a rational mix proportion can effectively improve the microstructure and mechanical properties of the ternary RM-based cementitious material.

Keywords: red mud; blast furnace slag; fly ash; mechanical properties; microstructure; fractal dimension

Check for updates

Academic Editor: Carlo Cattani

Received: 18 March 2026
Revised: 19 April 2026
Accepted: 21 April 2026
Published: 22 April 2026

Copyright: © 2026 by the authors. Licensee MDPI, Basel, Switzerland. This article is an open access article distributed under the terms and conditions of the Creative Commons Attribution (CC BY) license.

1. Introduction

Red mud (RM), an industrial solid waste generated in the production of alumina, yields approximately 1–2 tons of RM for every ton of alumina produced. To date, the global stock of RM has exceeded 5 billion tons and continues to rise at a rate of about 150 million tons per year [1,2], yet the overall utilization rate remains below 15% [3]. RM storage typically requires large storage yards that occupy substantial land resources. Due to its strong alkalinity, it can cause alkaline contamination of surrounding soils and water bodies, seriously affecting human living environments [4]. At present, excessive carbon

dioxide emissions have become a key problem restricting the smooth implementation of the "dual-carbon" strategy. The effectiveness and progress of the cement industry's carbon reduction directly affect the success of the dual-carbon strategy. Therefore, promoting the resource recovery of solid waste and developing low-carbon cementitious materials are of significant value for alleviating environmental pressure and implementing the national "dual-carbon" strategy. There is an urgent need to find safe and efficient pathways for the resource utilization of RM and to improve its overall utilization rate. Currently, approaches for the resource utilization of RM mainly include the preparation of construction materials, supplementary cementitious materials, soil conditioners, wastewater treatment, and the manufacture of glass and ceramics [5–9]. Among these, the use of RM in construction material production is considered the most promising and economically impactful pathway due to its large production volume, high comprehensive utilization rate, and relatively low cost.

RM-based cementitious materials, as a type of solid-waste construction material, are typically prepared using RM as the main component with supplementary solid wastes such as FA, BFS, steel slag, and desulfurization gypsum. An increasing number of researchers are focusing on the combined fabrication of cementitious materials using various types of solid waste. Among them, binary RM-based cementitious systems (RM plus BFS) have been studied more extensively; samples often exhibit excellent early strength but slower long-term strength development, with moderate overall performance. Zakira et al. [10] studied the preparation of high-strength geopolymers from RM–BFS and found that, under alkaline activation, a geopolymer made from a 50% RM–slag blend achieved a strength as high as 66 MPa. Tian et al. [11] studied the microstructural performance of Bayer RM–BFS cementitious materials and found that a proper dosage of RM promotes the alkali activation of slag, generating calcium aluminate and hydrated calcium silicate and calcium aluminosilicate, which increases the secondary hydration peak of the blend. In recent years, based on binary RM-based cementitious systems, some researchers have begun to explore the overall performance of multicomponent RM-based cementitious materials. By introducing FA, desulfurization gypsum, phosphogypsum, manganese residue, and other ternary or quaternary combinations, constructing multicomponent RM-based cementitious systems can improve the inherent deficiencies of single waste materials and further enhance the material's overall performance. Li et al. [12] studied the polymerization mechanism of RM, ultrafine FA, and BFS composites. The addition of RM lengthens the setting time, while the fluidity and compressive strength decrease; gel products such as C-(A)-S-H, AFt, and N-A-S-H are present in the composite material. The composite material exhibits fewer microcracks and a denser matrix structure. Zhang et al. [13] studied roadbed materials prepared from electrolytic manganese residue, RM and carbide residue, finding that ternary solid-waste roadbed materials exhibit stronger durability, under synergistic action, more hydration products are produced, demonstrating excellent pore distribution and microstructure. Wang et al. [14] investigated ternary RM-based cementitious materials comprising RM, desulfurization gypsum, and FA. In an alkaline environment, the three materials show significant synergy, promoting hydration reactions and producing more C-(A)-S-H and AFt, thereby giving good ability to immobilize Na^+. When the solid-waste contents reach 50%, the materials exhibit optimal mechanical properties that meet the strength standards of ordinary Portland cement (42.5 MPa). Zhang et al. [15] compared the synergistic effects of multicomponent binders made of red mud, blast furnace slag, steel slag, and desulfurization gypsum and found that, compared with binary and ternary binders, the quaternary binder exhibited superior setting time and compressive strength. The addition of steel slag and desulfurization gypsum can improve the uniformity of the slurry matrix, making the slurry denser. Moreover, the inert components of steel

slag can serve as fine aggregates to fill the pores, further improving the microstructure of the matrix. Cui et al. [16] studied quaternary red-mud-based cementitious materials composed of red mud, steel slag, fly ash, and phosphogypsum and found that the overall performance of the quaternary red-mud-based cementitious materials was better than that of conventional binary and ternary materials. The four materials exhibit a synergistic effect, significantly increasing the content of hydration products and forming a denser matrix structure. Compared with traditional cement, multicomponent RM-based cementitious materials align with green building material standards.

The above mentioned related studies show that by formulating theoretical designs for multiple solid-waste materials, low-carbon preparation processes, and environmental safety assessments, the synergistic relationship between the chemical composition, physical properties, and hydration behavior of different solid-waste materials can be precisely grasped. This can fully exploit the resource utilization potential of red mud and other solid-waste materials, playing a significant role in the sustainable development of green and low-carbon building materials and the achievement of carbon reduction targets [17]. The research results not only provide new paths for the large-scale, harmless, and resourceful utilization of industrial solid-waste materials such as red mud but also solve the problem of excessive CO_2 emissions during traditional cement production, which causes air pollution. This provides practical technical support for the implementation of the national "dual-carbon" strategy and the construction of ecological civilization.

However, the multicomponent nature of RM-based cementitious materials results in an intricate internal pore structure inside the material matrix. Using microstructural techniques, including scanning electron microscopy and nuclear magnetic resonance, can qualitatively or quantitatively describe the microstructure from a single dimension—surface morphology or pore structure, and it is difficult to comprehensively reflect the irregularity of pores inside the material. Fractal theory, as a reliable approach to describing complex disordered structures, quantifies the complexity of the microstructure or pore distribution into a fractal dimension, thereby revealing the evolution of pore structure more clearly [18–20]. Han et al. [21] found in their research on fly ash–cement composites that high temperature and mechanical grinding can increase the activity of raw materials, which helps the matrix form a denser microstructure, thereby increasing the fractal dimension obtained from mercury intrusion data. The change in the fractal dimension can be used to predict the trend of pore characteristics such as porosity and pore volume. Ren et al. [22] discovered in their study on the pore structure of concrete that the pore structure of concrete has obvious fractal characteristics. The NMR fractal dimension can be used as an important quantitative indicator of absorption performance; the larger the fractal dimension, the higher the absorption coefficient. Zheng et al. [23] investigated the fracture characteristics of fiber-reinforced concrete and found that the extent of microcrack propagation can be predicted by the fractal dimension. The larger the fractal dimension, the higher the degree of microcrack propagation, and the corresponding mechanical properties of the material decrease accordingly. Xue et al. [24] studied the mechanical properties of steel slag concrete and found that there is a clear correlation between the fractal dimension obtained from mercury intrusion data and the mechanical parameters and material strength. Variations in the fractal dimension can therefore be used to evaluate and predict the superiority or inferiority of the material's macroscopic performance. Existing studies have shown that mixed materials such as cement–limestone powder, coal gangue powder-improved expansive soil, and zeolite powder mortar all have obvious fractal characteristics [25,26]. The fractal dimension can reflect the complexity of the pore structure and its evolution law, thereby establishing a quantitative relationship between the microstructure characteristics and

material properties, and providing a more comprehensive theoretical basis for elucidating their intrinsic mechanism [27–29].

To enhance the utilization of RM and produce high-performance cementitious materials aligned with green and environmental standards, this study employs Bayer RM as the primary raw material, combined with BFS and FA to prepare ternary RM-based cementitious materials. Based on the macroscopic mechanical properties, fractal theory is applied to investigate the influence of different solid-waste contents on the microstructure of the RM-based cementitious materials across multiple scales. Through quantitative analysis, the intrinsic relationship between macroscopic mechanical parameters and microstructure is revealed. The research findings can provide a theoretical basis for the resource utilization of RM in construction materials.

2. Materials and Methods

2.1. Materials

2.1.1. Materials Properties

The raw materials used in the tests are RM, BFS, and FA. The appearances of the three materials are shown in Figure 1. RM was taken from Aluminum Mining Co., Ltd. in Zhengzhou City, China. The dried lump RM was crushed using a ball mill (Wzm-3L instrument, Suqian Ruili Xinke E-Commerce Co., Ltd., Suqian, China) to improve its activity. The BFS was purchased from Tianrui Building Materials Co., Ltd., in Zhengzhou City, China, and meets the national standard S95 grade [30]. FA was purchased from Jinrui New Materials Co., Ltd. in Zhengzhou City, China. The particle size distribution curves, microstructural morphology, and main chemical compositions of the three materials were determined, respectively, by a laser particle size analyzer (Malvern Mastersizer 3000, Spectra Group UK, Malvern, UK), XRF (Panalytical Axios, Hangzhou Information Technology Co., Ltd., Hangzhou, China), and SEM, as shown in Figures 2 and 3 and Table 1.

Table 1. The main chemical components of materials.

Materials	Main Chemical Composition and Content/%						
	Al_2O_3	Fe_2O_3	SiO_2	CaO	Na_2O	K_2O	SO_3
Red Mud	25.33	21.80	15.75	10.42	7.52	1.77	1.50
Blast furnace slag	14.50	0.43	26.95	43.62	0.38	0.42	2.19
Fly Ash	36.8	0.85	45.1	4.5	0.75	0	0



(**a**) (**b**) (**c**)

Figure 1. Raw material morphology (**a**) RM, (**b**) BFS, (**c**) FA.

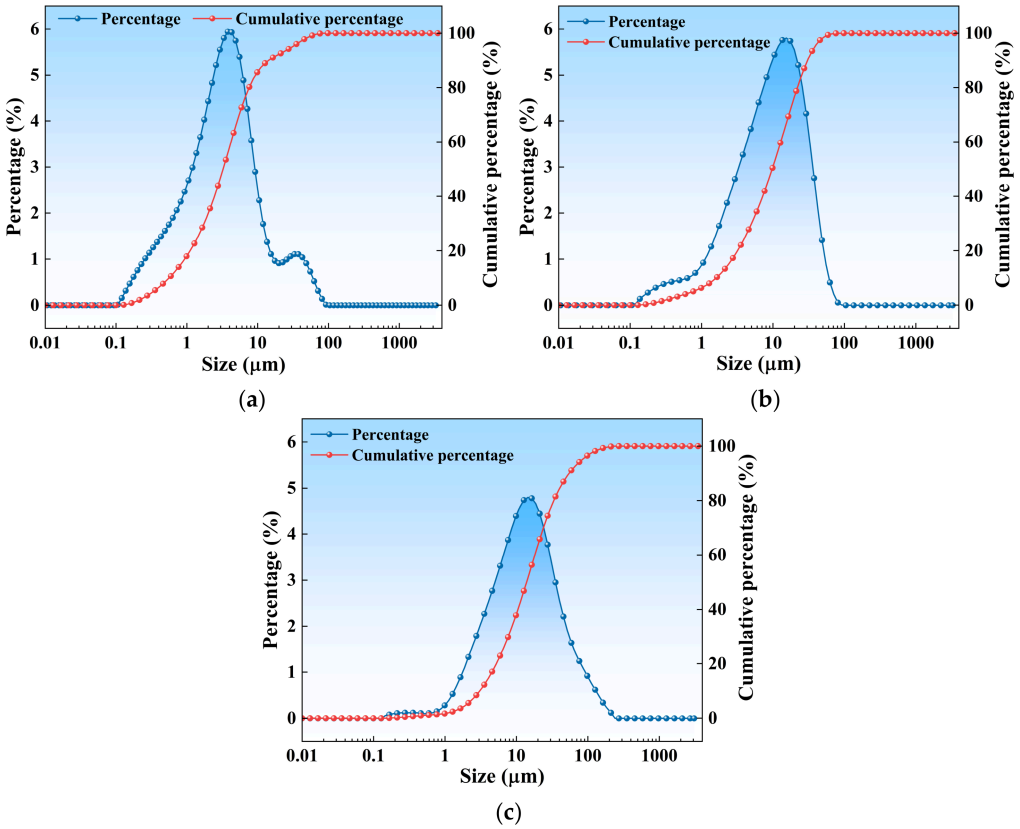


Figure 2. Particle size distribution curve (**a**) RM, (**b**) BFS, (**c**) FA.

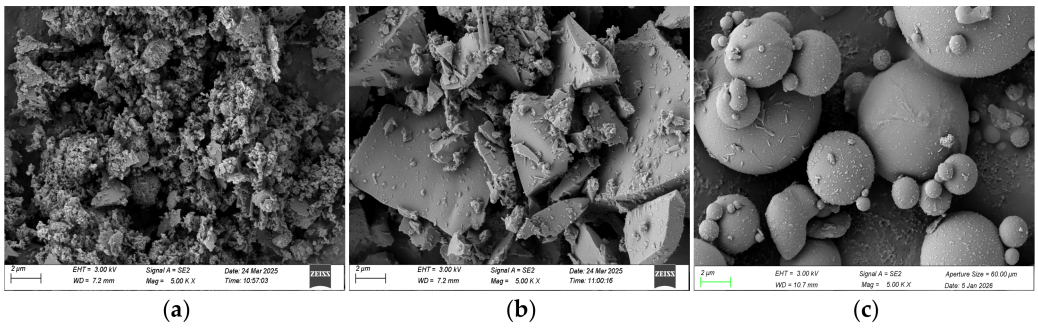


Figure 3. SEM images of materials (**a**) RM, (**b**) BFS, (**c**) FA.

Figure 2 presents the particle size distribution curves of the raw materials. The three raw materials have relatively uniform overall particle size distributions and large specific surface areas. The microstructures of the three materials are shown in Figure 3. As shown in Figure 3, RM mainly consists of agglomerated particles, with some fine particles adsorbed on the agglomerates; the surface is rough and irregular. The BFS presents an amorphously distributed blocky or flaky structure [31], with large pores between the particles. The FA appears as gray-black agglomerates, composed of spherical particles with uneven size distribution, which contain large agglomerated particles, and the overall structure is relatively loose. The main chemical compositions of the three raw materials are shown in Table 1. The RM has high contents of Al_2O_3, Fe_2O_3, and SiO_2, indicating a high content of aluminosilicates in the RM, demonstrating its potential as a geopolymer [32]. The BFS has the highest CaO content, accounting for 43.62%, which aligns with the characteristics of BFS as a high-calcium cementitious material and can provide an ample calcium source for the solid-waste system [33]. Additionally, the combined proportion of Al_2O_3 and SiO_2 exceeds 41%, which can accelerate the polymerization reaction in the material [34]. The

aluminosilicate content in the FA is as high as 81.9%, providing sufficient raw materials for subsequent reactions [35].

2.1.2. Alkali Activator

The alkali activator used in the experiments was prepared by mixing NaOH and water glass. The alkali activator materials are shown in Figures 4 and 5. NaOH is in the form of flake particles with a purity exceeding 98%. Water glass mainly consists of sodium silicate, with the chemical formula $Na_2O{\cdot}mSiO_2{\cdot}nH_2O$, where m represents the modulus. The mass fractions of SiO_2 and Na_2O in the liquid sodium silicate are 27.3% and 8.54%, respectively. The alkaline activator needs to be prepared one day in advance of the experiment and allowed to cool indoors for 24 h before use.



Figure 4. Sodium silicate.



Figure 5. Sodium hydroxide.

2.2. Specimen Preparation

Our preliminary group experiments determined the optimal binary RM–slag cementitious material ratio as a mass ratio of RM to BFS of 5:5, with an alkali activator modulus of 1.8, a liquid-to-solid ratio of 0.3, and an alkali activator content of 10% of the total

cementitious material; at this mix proportion, the binary red-mud-based cementitious material exhibits excellent mechanical properties. This study uses that baseline to study the influence of different FA contents on the mechanical properties of the ternary RM–slag–FA cementitious system by designing three schemes (A, B, and C) to adjust the raw material proportions. Scheme A: Simultaneously reduces the proportions of RM and BFS to increase FA content. Scheme B: Reduces only the RM amount while keeping the BFS amount unchanged, thereby increasing FA content. Scheme C: Reduces only the BFS amount while keeping RM constant, thereby increasing FA content. The specific experimental mix proportions are shown in Table 2. The detailed sample preparation process is as follows:

Table 2. Test mix ratio at different FA contents.

Experimental Scheme	Rud Mud Content/%	Blast Furnace Slag Content/%	Fly Ash Content/%	Liquid-Solid Ratio	Alkali Activator Modulus	Alkali Activator Content	Curing Age
A	47.5	47.5	5	0.3	1.8	10%	7 d/28 d
	45	45	10				
	42.5	42.5	15				
	40	40	20				
B	45	50	5	0.3	1.8	10%	7 d/28 d
	40	50	10				
	35	50	15				
	30	50	20				
C	50	45	5	0.3	1.8	10%	7 d/28 d
	50	40	10				
	50	35	15				
	50	30	20				

(1) Weigh out RM and BFS according to the designed mix proportion and place them into a paste mixer (planetary mixer, Cangzhou Xinglan Construction Instrument Co., Ltd., Cangzhou, China) for low-speed stirring for 5 min to ensure thorough blending. (2) Calculate the masses of NaOH particles and liquid sodium silicate according to the alkali activator modulus, and pre-mix to prepare the alkali activator. (3) After the low-speed stirring is complete, add the alkali activator and water, and mix at high speed for 2 min to ensure even blending of the two materials. (4) Put the mixed material into the corresponding molds and use a vibration table to reduce air bubbles inside the specimens and ensure compactness. (5) Cast the specimens into cubes of 40 mm × 40 mm × 40 mm and prisms of 40 mm × 40 mm × 160 mm. Seal the molds with plastic wrap and cure for 24 h at room temperature, then demold and place the specimens in a standard curing room for cure until 7 days and 28 days, respectively. After the curing ages are completed, conduct the relevant mechanical property and microstructural tests. The detailed specimen preparation procedure is shown in Figure 6.

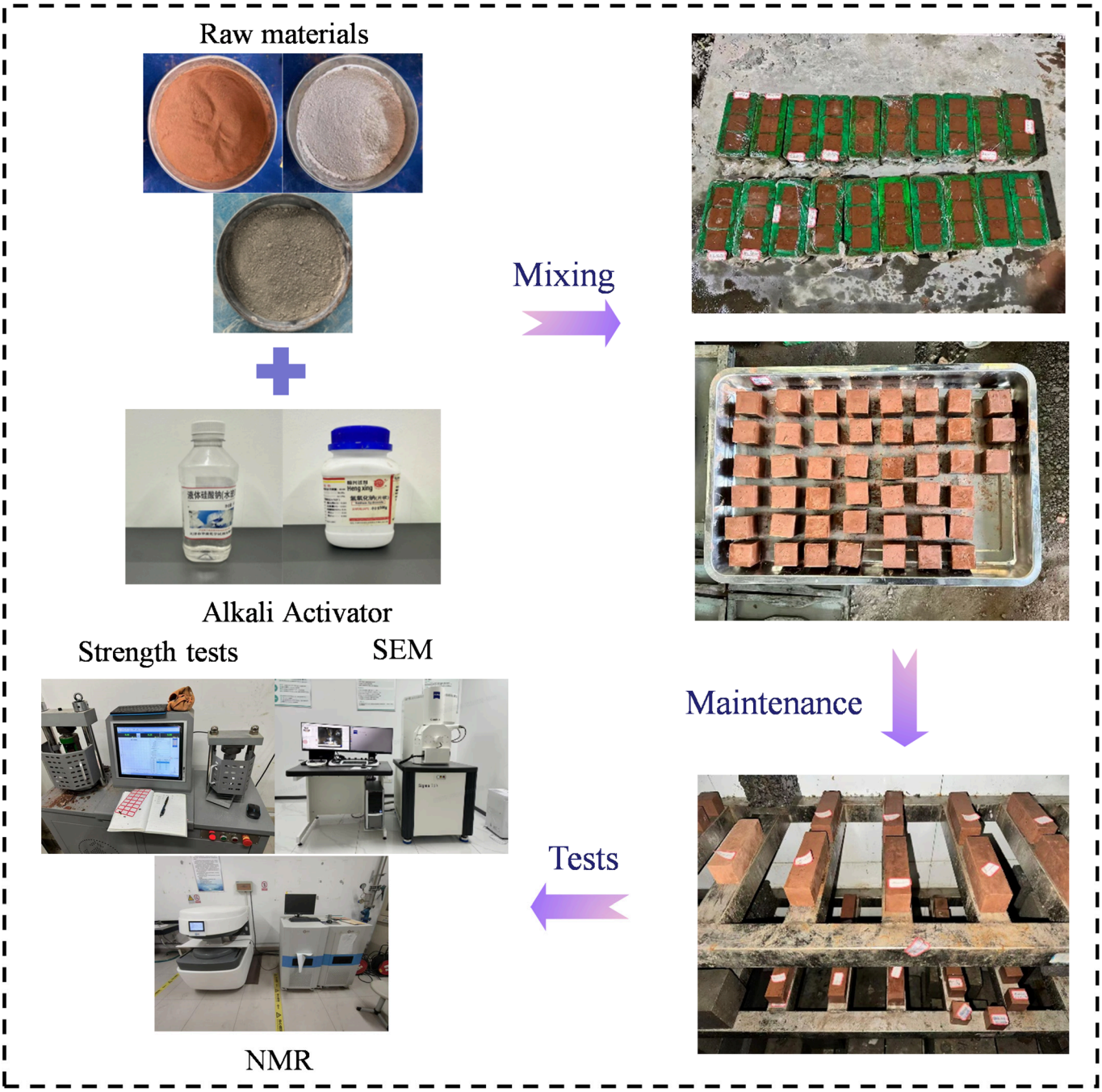


Figure 6. Specimen preparation flowchart.

2.3. Experimental Methods

2.3.1. Compressive and Flexural Strength Tests

Compressive strength tests were conducted on specimens cured for 7 and 28 days using a fully automatic compression testing machine (DYE-300S instrument, Beijing Laituo Gaoke Instrument Co., Ltd., Beijing, China). The loading mode was set to stress-controlled with a loading rate of 2400 N/s, and loading continued until specimen failure. The compressive strength results were taken as the average of three specimens with identical mix proportions. The process for flexural strength testing was essentially the same as that for compressive strength testing. The three-point bending method is adopted, with GB/T 17671-2021 used as the reference standard [36]. Flexural tests were performed on specimens at 7 and 28 days by placing the specimens on the supporting platform of the flexural test setup, ensuring

that the load from the testing machine was applied evenly to the center of the specimen until fracture occurred.

2.3.2. Scanning Electron Microscopy and Energy Dispersive Spectrometer Tests

After performing compressive tests on the specimens cured for 28 days, representative specimen fragments were selected and immersed in anhydrous ethanol for two days to halt the hydration reaction. Before SEM analysis, the samples were placed in a 60 °C drying oven for 24 h to dry them, then sputter-coated with gold to prevent negative effects from surface charge accumulation. The experiments employed a ZEISS Sigma 300 scanning electron microscope (SEM) manufactured by ZEISS in Oberkochen, Baden-Württemberg, Germany, to analyze the microstructural morphology of the samples and combine an Xplore 30 energy-dispersive spectroscopy (EDS) system (Oxford Xplore 30, Oxford Instruments Technology (Shanghai) Co., Ltd., Shanghai, China) to perform scans at representative points in SEM images to determine the elemental distribution of the samples.

2.3.3. Nuclear Magnetic Resonance Test

The Nuclear magnetic resonance (NMR) tests are performed using the MesoMR12-060H-I (MR) type NMR instrument produced by Suzhou Neway Analytical Instrument Co., Ltd., Suzhou, China. The MesoMR12-060H-I (MR) type nuclear magnetic resonance equipment was used to perform non-destructive pore structure characterization on the samples cured to the specified age. Before testing, the samples are vacuum-saturated for 24 h to fill the pores with water, thereby improving the accuracy of the experiments. Subsequently, NMR detection was carried out to obtain the pore size distribution, which was used for subsequent pore structure analysis and fractal characterization.

3. Test Results

3.1. The Influence of Different FA Contents on the Mechanical Properties of RM-Based Cementitious Materials Under Scheme A

The compressive and flexural strengths of RM-based cementitious materials with different FA contents under Scheme A are shown in Figure 7. As shown in Figure 7, at the curing age of 7 days, the compressive strength first increases and then decreases with the increase in FA content. This trend occurs because during the early curing period, a small amount of FA acts as a micro-aggregate to fill internal pores and improve the compactness of the material. As the FA content increases further, the filling effect inside the matrix reaches a threshold and cannot further improve the matrix structure by reducing pores. Meanwhile, the reduction in high-calcium slag content leads to a decrease in the compressive strength of RM-based cementitious materials at high FA contents. However, at 28 days, the compressive strength shows a significant upward trend with increasing FA content. Compared with the 28-day strength of 40.4 MPa without FA, the 28-day compressive strengths at different FA contents are 45.1 MPa, 44.9 MPa, 47.7 MPa, and 50.8 MPa, corresponding to strength increases of 11.6%, 11.1%, 18.1%, and 25.7%, respectively. The reason is that in an alkaline environment, the active silica within FA undergoes geopolymerization and hydration with calcium and sodium ions, promoting the generation of C-(A)-S-H gels and further refining the pore structure [37]. This indicates that FA addition helps enhance long-term strength.

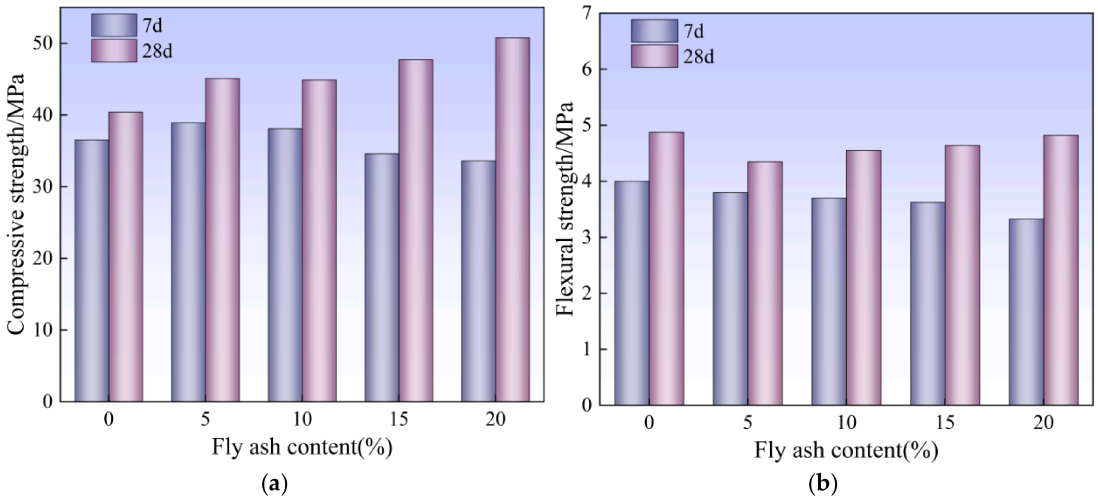


Figure 7. Compressive and flexural strengths at different FA contents under Scheme A. (**a**) Compressive strength. (**b**) Flexural strength.

However, the overall flexural strength at different FA contents decreases compared to that without FA incorporation. Specifically, as FA content increases, the flexural strength at 7 days generally decreases, while at 28 days it first decreases and then increases. Although the 28-day compressive strength shows a marked improvement, the flexural strength remains comparatively stable. This is because the reaction products of FA can enhance the matrix density and improve resistance to axial compression, but their contribution to material toughness and crack propagation resistance is limited. There may be partially unreacted particles and weak interfacial zones that become hotspots for crack initiation and propagation under bending loads, thus inhibiting enhancements in flexural performance. Overall, at 20% FA content, the compressive strength is the highest, and the flexural strength is essentially unchanged compared with the binary system. The ternary system RM–BFS–FA demonstrates the best overall mechanical performance. Therefore, 20% FA content is chosen as the optimal proportion for Scheme A.

3.2. The Influence of Different FA Contents on the Mechanical Properties of RM-Based Cementitious Materials Under Scheme B

The variation patterns of compressive and flexural strengths of RM-based cementitious materials with different FA contents under Scheme B are shown in Figure 8. From Figure 8, at 7 days of age, the compressive strength generally shows a decreasing trend as the FA content increases. One reason is that the reduction in RM content weakens the overall alkalinity of the ternary system, thereby slowing the early hydration of slag and FA, resulting in a lower content of cementitious substances in the specimens, making it difficult to form sufficient bonding strength [38]. Another reason is that RM particles have a fine particle size and a large specific surface area, which can provide a good micro-aggregate effect in the early stage of the specimens, making the internal structure of the specimens denser and reducing the adverse effects of pores on strength. As the RM content decreases, this filling effect gradually weakens, potentially leading to an increase in internal porosity and consequently a decline in early compressive strength.

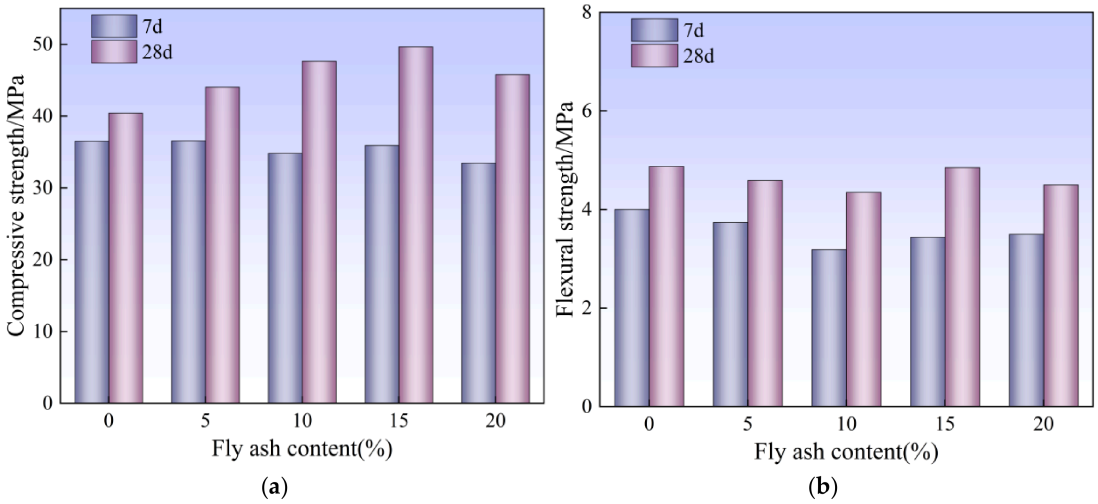


Figure 8. Compressive and flexural strengths at different FA contents under Scheme B. (**a**) Compressive strength. (**b**) Flexural strength.

At 28 days, with the reduction in RM content and the increase in FA content, the compressive strength overall rises significantly. The reason is that FA contains a substantial proportion of silica. During the later stages of the reaction, the pozzolanic activity of FA gradually activates, generating a large amount of cementitious material to connect pores and refine the matrix structure, thereby significantly improving the later-stage compressive strength of the material. However, the overall flexural strength under Scheme B shows a trend similar to Scheme A, and the increase in FA content does not cause a noticeable change in flexural strength. At 15% FA content, the Scheme B RM–BFS–FA ternary system exhibits the best overall mechanical performance. Therefore, 15% FA content is chosen as the optimal mix proportion for Scheme B.

3.3. The Influence of Different FA Contents on the Mechanical Properties of RM-Based Cementitious Materials Under Scheme C

The compressive and flexural strengths of RM-based cementitious materials with different FA contents under Scheme C are shown in Figure 9. From Figure 9, with the decrease in BFS content, the early-stage compressive and flexural strengths decline significantly. The reason is that BFS, as a highly active geopolymer raw material, has much higher early hydration activity than FA. The reduction in BFS content directly leads to a decrease in early hydration products, resulting in a lower content of cementitious substances within the system. At 28 days, the compressive and flexural strengths show a trend of decreasing first and then increasing. The reason is that the later strength contribution from FA cannot compensate for the loss of early strength contribution from highly active slag, resulting in an overall strength drop. When the FA content is higher, its substantial pozzolanic activity and micro-aggregate effect become dominant, driving the increase in strength in the later stage. However, the flexural strength overall shows a decreasing trend because, under alkaline activation by RM, the hydration products predominantly include needle-like AFt and fibrous C-S-H gels, which can weave into a continuous tough backbone inside the specimen [39]. As FA content increases, its spherical particles with smooth surfaces form flocculent C-S-H cementitious materials, which provide weaker cohesive effects compared to the hydration products of slag. At a 15% FA content, the ternary RM–slag–FA system under Scheme C exhibits the best overall mechanical performance. Therefore, 15% FA content is chosen as the optimal mix proportion for Scheme C.

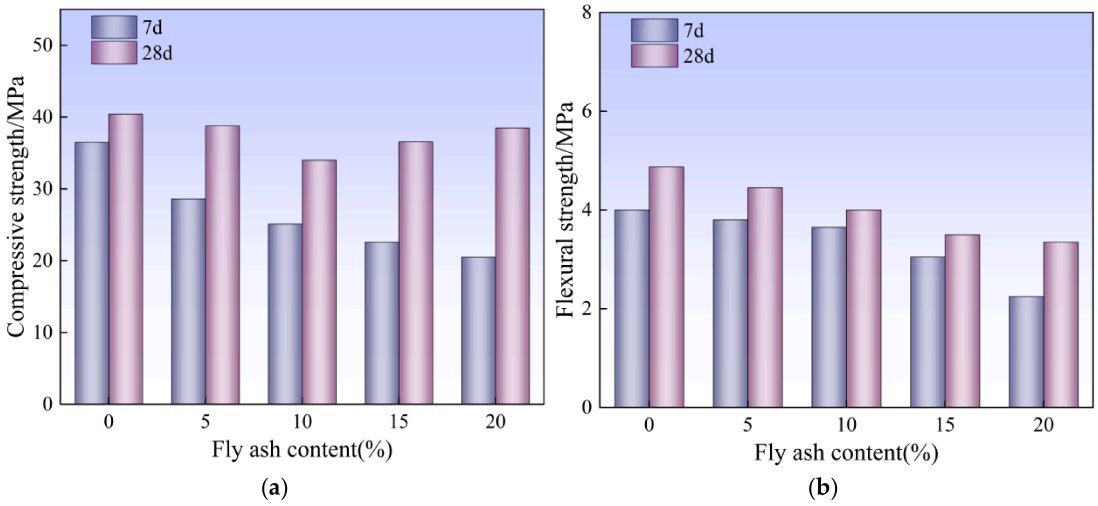


Figure 9. Compressive and flexural strengths at different FA contents under Scheme C. (**a**) Compressive strength. (**b**) Flexural strength.

Based on the comparative analysis of compressive and flexural strengths in a ternary RM-based cementitious material system under Schemes A, B, and C, by changing the FA content in different ways, the results show that under Scheme B, if RM content is decreased alone while FA content is increased, the later-age compressive strength of the ternary RM system increases significantly, but the overall utilization rate of RM is low. From Scheme C, if the BFS content is reduced alone, the compressive and flexural strengths of the ternary RM system show a downward trend. Integrating Schemes A, B, and C, if RM and slag contents are reduced simultaneously, the flexural strength of the ternary system remains generally stable, but the later-age compressive strength is significantly improved, with an increase of about 25%. Meanwhile, the utilization rate of RM is higher. Therefore, the experiment selected Scheme A with a mass ratio of RM:slag:FA of 4:4:2 as the optimal content for the ternary RM cementitious system.

4. The Microstructural Study of RM-Based Cementitious Materials

4.1. Analysis of SEM and Elemental Composition Results of Ternary RM-Based Cementitious Materials

The microtopography of the ternary RM-based cementitious material is shown in Figure 10. From Figure 10, because there are many SEM images for the ternary RM-based cementitious material, this section only analyzes SEM images of Schemes A, B, and C with FA contents of 20%, 15%, and 15%, respectively. Compared with the binary system (Figure 9a), the ternary RM-based cementitious material shows increased gel content, and the porosity and pore size within the matrix are significantly reduced, leading to improved densification. When FA is incorporated into the RM–BFS binary system, during the later reaction stages, a large amount of reactive Si and Al species in the FA gradually dissolve to form free Si^{4+} and Al^{3+}, providing ample raw materials for hydration. Meanwhile, the pozzolanic reaction of FA consumes hydroxide ions and generates large quantities of cementitious materials, effectively filling the pores in the matrix [40]. Furthermore, unreacted FA particles can act as nucleation carriers for hydration products, providing abundant nucleation sites [41], accelerating the hydration rate, and thereby improving the overall mechanical performance of the material.

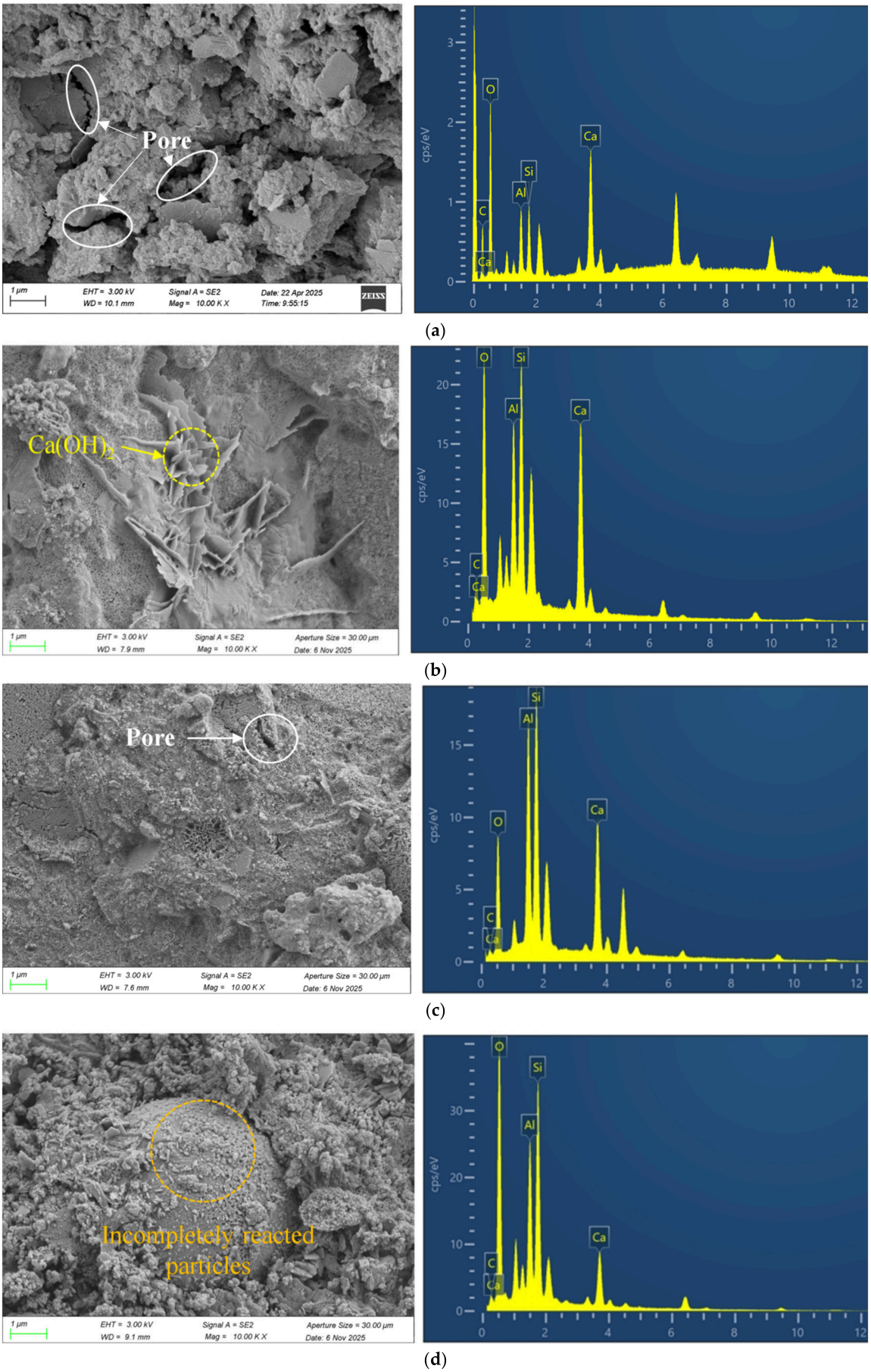


Figure 10. SEM images of RM-based cementitious materials. (**a**) 0% FA. (**b**) Scheme A. (**c**) Scheme B. (**d**) Scheme C.

Specifically, in Scheme A, the SEM image shows abundant interwoven C-S-H gel forming a continuous network, with RM and BFS particles tightly encapsulated by the gel, and interparticle pores effectively filled, leaving only a few tiny pores. In Scheme B, the networked gel is also fairly uniformly distributed. Although the FA content is slightly lower than in Scheme A, the hydration products of RM and BFS can still connect well with the gel formed by the early hydration of FA, without significant particle agglomeration or large pore defects. In the SEM image of Scheme C, because the BFS content is relatively low, while BFS is a core source of hydration products in the ternary system, the insufficient BFS content results in a relatively small total amount of hydration gel, and the SEM image shows a noticeably lower gel network density than in Schemes A and B, with many unreacted RM particles adhering to the FA surface, resulting in poor overall densification of the material.

To further study the influence of FA content on the elemental composition of the RM-based cementitious material, changes in the elemental composition of the material with different FA contents were analyzed through EDS energy spectrum testing, the specific composition of material elements is shown in Table 3. The Ca/Si ratios at different FA contents are 3.93, 1.03, 1.60, and 0.51, respectively. The Ca/Si ratio decreases significantly after the addition of FA, which may be because the addition of FA provides abundant reactive silicon and aluminum species that accelerate the formation of the cementitious material, thereby consuming the calcium and silicon sources present in the raw materials. Among them, Scheme C has the lowest Ca/Si ratio [42,43], which is due to the reduction in BFS content and increase in FA content, leading to fewer calcium sources inside the material, with a large amount of unreacted FA causing the silicon content in the matrix to rise significantly and resulting in a lower Ca/Si ratio.

Table 3. EDS elemental composition table.

Elemental/w%/	0% FA	Scheme A—20% FA	Scheme B—15% FA	Scheme C—15% FA
C	21.85	13.31	20.68	13.17
O	47.96	40.56	49.23	58.21
Al	4.79	13.21	6.6	9.21
Si	5.15	16.25	9.02	12.83
Ca	20.25	16.68	14.47	6.58
Ca/Si	3.93	1.03	1.60	0.51

4.2. Fractal Analysis of SEM Images of RM-Based Cementitious Materials

Due to the complex microstructure of multicomponent RM-based cementitious materials, SEM images alone can only observe microstructural changes at a superficial level and are difficult to explain changes in the internal structure quantitatively. The box-counting method is employed to quantify SEM images into fractal dimensions, thereby establishing a quantitative basis for studying the evolution of their microstructure [44]. The specific processing workflow of the box-counting method is illustrated in Figure 11, and the specific calculation formula is as follows.

$$D = -\lim_{\delta \to 0} \frac{\ln N(\delta)}{\ln \delta} \quad (1)$$

where δ represents the edge length of the box, $N(\delta)$ represents the number of grid boxes, and D represents the fractal dimension.

The microstructure of RM-based cementitious materials was characterized using fractal analysis using SEM combined with the box-counting method. The box-counting fractal dimensions of the RM-based cementitious materials are shown in Figure 12 and Table 4. From Figure 12 and Table 4, the box-counting fractal dimension values range from 1.7561

to 1.8316, with correlation coefficients R^2 all greater than 0.99, meeting the theoretical value for two-dimensional fractal dimensions. Compared with the binary RM-based cementitious material, the ternary RM-based cementitious material shows a significantly larger fractal dimension, which is because the introduction of FA promotes the formation of gel materials inside, altering the original matrix structure and increasing the complexity of the RM-based cementitious material, thereby increasing the fractal dimension [45].

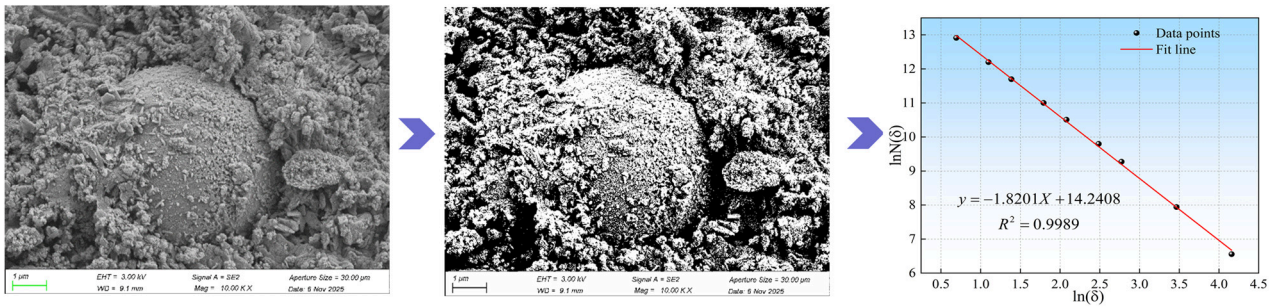


Figure 11. Box-counting method operation process. (**a**) SEM raw grayscale image. (**b**) Binary conversion. (**c**) Data fitting.

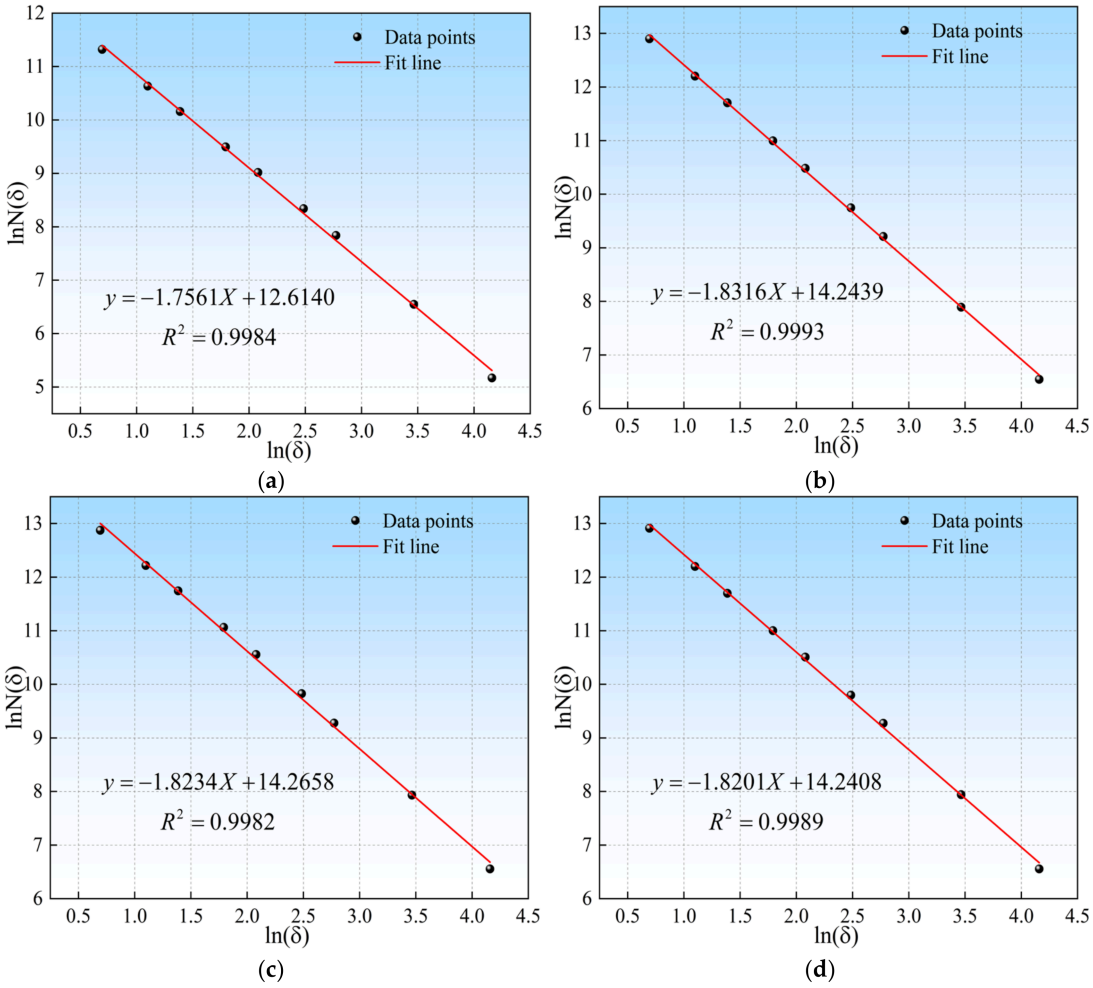


Figure 12. Box-counting fractal dimension of sem images. (**a**) 0% FA. (**b**) Scheme A. (**c**) Scheme B. (**d**) Scheme C.

Table 4. Box fractal dimension table.

Specimen Number	Fitting Curve	Fractal Dimension	Correlation Coefficient
0% FA	y = −1.7561x + 12.6140	1.7561	0.9984
Scheme A—20% FA	y = −1.8316x + 14.2439	1.8316	0.9993
Scheme B—15% FA	y = −1.8234x + 14.2658	1.8234	0.9982
Scheme C—15% FA	y = −1.8201x + 14.2408	1.8201	0.9989

4.3. NMR Analysis of RM-Based Cementitious Materials

Due to the complex and variable pore structure of multicomponent RM-based cementitious materials, the pores in these materials are classified into harmless pores (<20 nm), less harmful pores (20–50 nm), and harmful pores (>50 nm) [46]. To further investigate the influence of FA content on the pore structure of RM-based cementitious materials, the T_2 spectra of RM-based cementitious materials with different FA contents are shown in Figure 13. With the incorporation of FA, the shape of the T_2 spectrum curve changes, shifting from an original three-peak distribution to a two-peak distribution, and none of the specimens with FA show harmful pores. The above analysis indicates that the addition of FA can improve the matrix structure by reducing the pores of alkali-activated cementitious materials by reducing the volume of harmful pores, leading to a denser microstructure in the RM-based cementitious materials. Compared with the 7-day curing age, as the curing age increases, the intensity of the first peak in the T_2 spectrum gradually decreases. This is due to the fact that with prolonged curing, FA provides ample active silica within the matrix, promoting polymerization and hydration reactions to generate abundant gel that optimizes the pore structure, and consequently reduces the signal intensity.

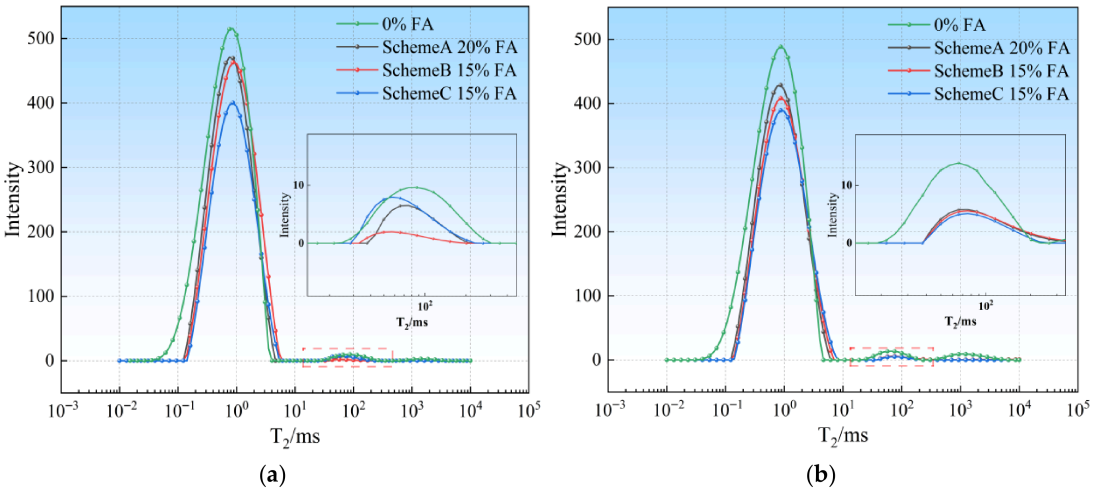


Figure 13. T_2 spectrum curve of RM-based cementitious material at different FA contents. (**a**) 7 d, (**b**) 28 d.

The pore size distribution characteristics of the RM-based cementitious materials are shown in Figure 14. From Figure 14, the proportion of internal pore sizes in the material decreases significantly after the incorporation of FA. The reason is that after FA partially replaces RM and slag, its finer particle size allows it to fully exert a micro-aggregate filling effect. As curing age increases, the overall pore size fraction continues to decrease, since the highly active silicon–aluminum components in FA are activated with age and undergo secondary reactions with the hydration products in the system, continuously generating more C-S-H gel to optimize the pore structure. Among them, compared to Schemes B and C, Scheme A exhibits a higher overall proportion of harmless pores. This may be attributed

to the increased amount of cementitious products formed within the matrix under the optimal mix proportion, leading to a denser microstructure and, consequently, a higher overall content of harmless pores.

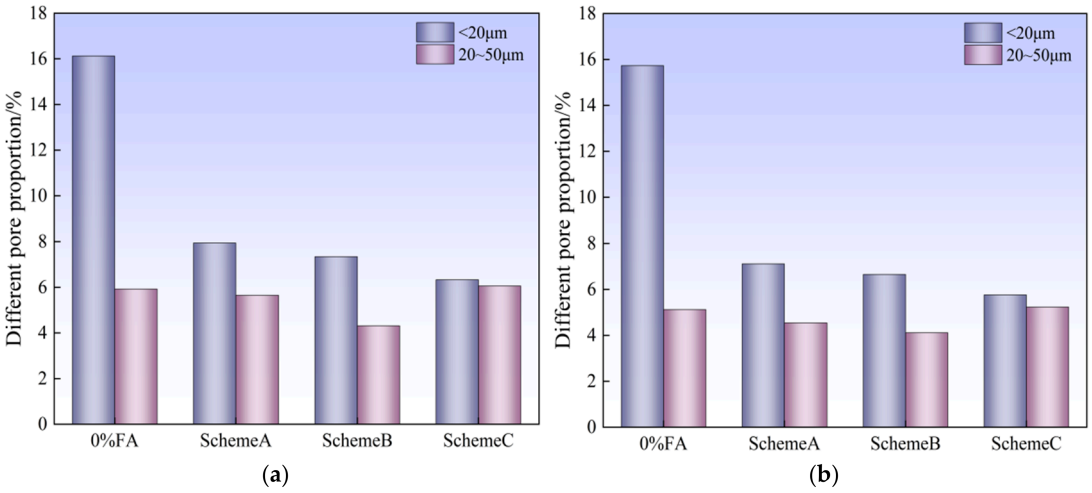


Figure 14. Proportion of different pore types in RM-based cementitious materials. (**a**) 7 d, (**b**) 28 d.

4.4. Fractal Analysis of NMR of RM-Based Cementitious Materials

Due to the disordered distribution and complex variability of pore shapes within cementitious materials, the application of fractal dimension can effectively quantify the complexity of the material's pores. NMR (Nuclear Magnetic Resonance) offers the advantage of non-destructive pore size detection. Therefore, NMR technology was employed to quantitatively characterize the fractal features of the pore structure in RM-based cementitious materials [47,48]. The specific calculation formula for the NMR fractal dimension is as follows [49]:

$$\lg S_V = (3 - D_V)\lg T_2 + (D_V - 3)\lg T_{2\max} \quad (2)$$

where T_2 is the transverse relaxation time, S_v is the ratio of the cumulative pore volume with relaxation time less than T_2 to the total pore volume, D_v is the fractal dimension, and $T_{2\max}$ is the maximum transverse relaxation time.

Compute the $\lg T_2$ and $\lg S_v$ double-log curves for the RM-based cementitious material using Formula (2), and the fractal dimensions corresponding to different pore types were computed through curve fitting according to the aforementioned pore classification, with the specific fractal dimension values presented in Table 5. From Figure 15, the overall shapes of the double-log curves are similar across FA contents, with the fractal dimensions for harmful pores > fractal dimensions for slightly harmful pores > fractal dimensions for harmless pores, indicating that larger pores have a higher pore-structure complexity [50]. In addition, in traditional Euclidean geometry, NMR fractal dimensions typically lie between 2 and 3, since the harmless pore fractal dimensions do not fall within this range, which lack physical significance and are thus not analyzed further [51]. From Table 5, after the incorporation of FA, the fractal dimensions for harmless and slightly harmful pores change considerably, but there is no clear upward or downward trend, while the fractal dimension for harmful pores shows an overall increasing trend. The reason is that FA, acting as a micro-aggregate, can directly fill harmful pores, exerting a more significant filling and connecting effect on the larger harmful pores [52]. Meanwhile, the aluminosilicates in the FA itself provide raw materials for later-stage secondary hydration reactions, generating abundant C-S-H gel that further bonds the pores and refines the structure [53,54]. This enhances the overall irregularity and structural complexity of the harmful pore interfaces.

Table 5. Nuclear magnetic fractal dimension under different aperture types.

Specimen Number	Harmless Pore		Less Harmful Pore		Harmful Pore	
	K_1	D_1	K_2	D_2	K_3	D_3
0% FA	3.0617	−0.0617	0.0891	2.9109	0.0046	2.9954
Scheme A—20% FA	2.1892	0.8108	0.3229	2.6771	0.0032	2.9968
Scheme B—15% FA	2.4797	0.5203	0.3561	2.6439	0.0035	2.9965
Scheme C—15% FA	2.2873	0.7127	0.3289	2.6711	0.0040	2.9960

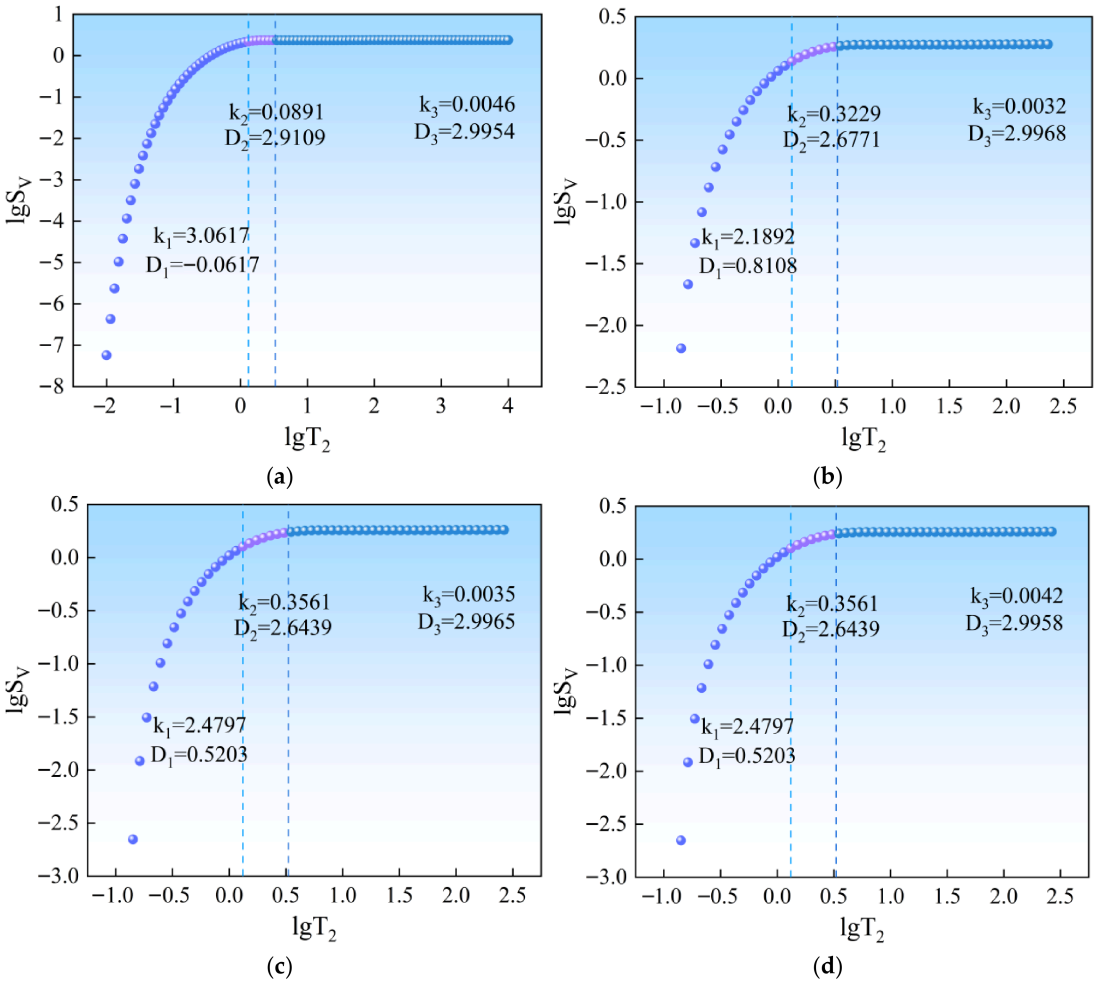
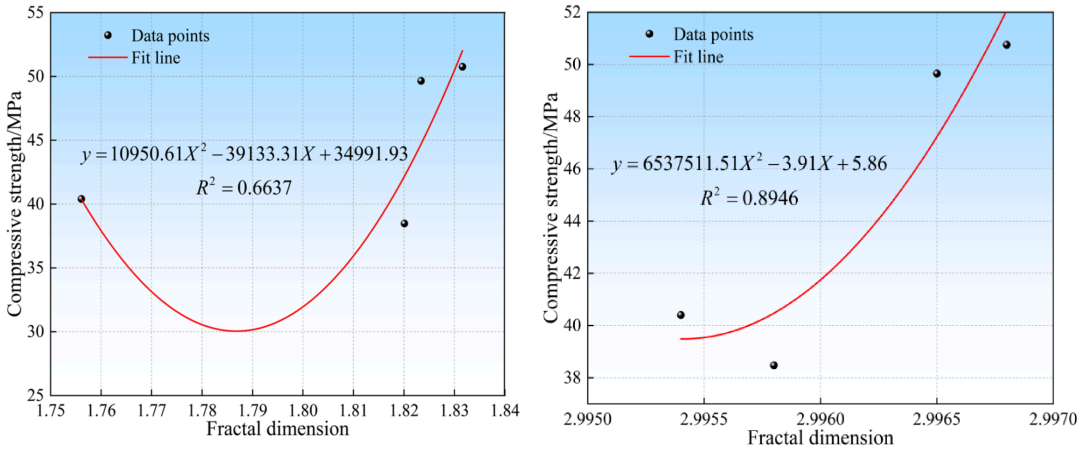


Figure 15. NMR fractal dimension of RM-based cementitious materials at different FA contents (**a**) 0% FA. (**b**) Scheme A. (**c**) Scheme B. (**d**) Scheme C.

4.5. Relationship Between Fractal Dimension and Compressive Strength

To further investigate the influence of microstructural changes on the mechanical properties of RM-based cementitious materials, mathematical models were established between box-counting fractal dimension, NMR fractal dimension, and compressive strength. The fitting curves of the box-counting fractal dimension and NMR fractal dimension with compressive strength are shown in Figure 16. From Figure 16, the relationships between box-counting fractal dimension, NMR fractal dimension, and compressive strength can be expressed using a binomial expression. As the box-counting fractal dimension value increases, the compressive strength shows an increasing trend, but the overall distribution is relatively scattered, exhibiting a weaker trend. In contrast, as the NMR fractal dimension value increases, the compressive strength demonstrates an increasing trend, and the fitting accuracy of the NMR fractal dimension is higher. The reason is that the box-counting fractal

dimension mainly reflects the spatial complexity at the apparent scale of the material, while two-dimensional image methods cannot fully characterize the spatial connectivity of pores [55]. Compared with the box-counting fractal dimension, the NMR fractal dimension can better capture local detailed features from a three-dimensional perspective and reflect the pore distribution across different scales. This provides a more reliable quantitative basis for material performance optimization and microstructural evolution.



(**a**) (**b**)

Figure 16. Fitting curves of different fractal dimensions and compressive strength. (**a**) Box-counting fractal dimension (**b**) NMR fractal dimension.

5. Conclusions

Through the study of the mechanical properties and microstructural evolution of ternary RM–BFS–FA cementitious materials, the optimal mix proportion for the ternary RM-based cementitious material was determined. Based on the analysis of compressive strength, flexural strength, and microstructure, combined with fractal theory, the evolution laws of the ternary RM-based cementitious material were revealed from a mesoscopic perspective. The main conclusions are as follows:

(1) The incorporation of FA can significantly enhance the later-age compressive strength of the material, while the flexural strength remains largely unchanged. The modification effect achieved by unilaterally reducing the content of either RM or slag to increase FA content is inferior to the approach of simultaneously reducing the contents of both RM and slag to increase FA content. When the mass ratio of RM, BFS, and FA is 4:4:2, the alkali activator modulus is 1.8, the liquid-to-solid ratio is 0.3, and the alkali activator accounts for 10% of the total cementitious materials, the mechanical performance is optimal while maintaining a high utilization rate of red mud. The 28-day compressive strength is about 25% higher than that of the binary RM–BFS cementitious material, reaching a strength of 50 MPa.

(2) Microscopic test results indicate that the incorporation of FA improves the densification of the matrix. On one hand, FA acts as a micro-aggregate, providing a physical filling effect. On the other hand, the high silica content in FA supplies ample raw materials for the later stages of hydration, increasing the formation of cementitious substances and reducing the Ca/Si ratio of the material. An abundant interwoven C-S-H gel is formed within the matrix, connecting the various component particles, optimizing the pore structure and improving the performance of the material.

(3) By fitting the fractal dimension with compressive strength, it was found that compared to the box-counting fractal dimension, the fitting accuracy of the NMR fractal dimension is higher. The reason is that NMR fractal dimension can better capture

local detail features from a three-dimensional perspective, enabling a more precise quantitative characterization of the changes in pore structure, thereby offering a more reliable quantitative basis for optimizing material performance and understanding microstructural changes.

Author Contributions: Writing—review and editing H.H.; data curation Y.Z.; writing—original draft preparation R.L.; methodology Q.Q.; conceptualization C.S. All authors have read and agreed to the published version of the manuscript.

Funding: This research received no external funding.

Data Availability Statement: Data is contained within the article.

Conflicts of Interest: Author Changbo Song was employed by the Power China Beijing Engineering Corporation Limited. The remaining authors declare that the research was conducted in the absence of any commercial or financial relationships that could be construed as a potential conflict of interest.

References

1. Tang, J.; Zhou, W.; Cai, X.; Zhang, D. Feasibility of upcycling red mud for low-CO_2 cement via calcination: A comparative study with FA and GGBFS based in China. *J. Clean. Prod.* **2024**, *476*, 143734. [CrossRef]
2. Archambo, M.; Kawatra, S.K. Red mud: Fundamentals and new avenues for utilization. *Miner. Process. Extr. Metall. Rev.* **2021**, *42*, 427–450. [CrossRef]
3. Liu, Y.; Zhang, L.; Xue, B.; Chen, L.; Wang, G.; Wang, J.; Zhu, G. Simulation of red mud/phosphogypsum-based artificial soil engineering applications in vegetation restoration and ecological reconstruction. *Sci. Total Environ.* **2024**, *951*, 175656. [CrossRef] [PubMed]
4. Wang, M.; Liu, X. Applications of red mud as an environmental remediation material: A review. *J. Hazard. Mater.* **2021**, *408*, 124420. [CrossRef]
5. Li, W.Y.; Zhang, Z.Y.; Zhou, J.B. Preparation of building materials from Bayer red mud with magnesium cement. *Constr. Build. Mater.* **2022**, *323*, 126507. [CrossRef]
6. Wang, F.; Xu, J.; Yin, H.; Zhang, Y.; Pan, H.; Wang, L. Sustainable stabilization/solidification of the Pb, Zn, and Cd contaminated soil by red mud-derived binders. *Environ. Pollut.* **2021**, *284*, 117178. [CrossRef] [PubMed]
7. Fang, W.; Zhou, Y.; Cheng, M.; Zhang, L.; Zhou, T.; Cen, Q.; Liu, Z. A review on modified red mud-based materials in removing organic dyes from wastewater: Application, mechanisms and perspectives. *J. Mol. Liq.* **2024**, *407*, 125171. [CrossRef]
8. Guo, J.; Cui, H.; Liu, M.; Chen, J.; Wen, M.; Wang, C.; Liu, S. Glass and glass-ceramics from red mud tailings: Understanding the evolution mechanism. *Ceram. Int.* **2023**, *49*, 27430–27438. [CrossRef]
9. Yuan, W.; Li, H.; Zhang, D.; Pan, T.; Li, Y.; Yan, Z.; Chang, N. Effects of Red Mud Incorporation on the High-Temperature Performance of Alkali-Activated Fly Ash. *J. Environ. Chem. Eng.* **2025**, *13*, 120061. [CrossRef]
10. Zakira, U.; Zheng, K.; Xie, N.; Birgisson, B. Development of high-strength geopolymers from red mud and blast furnace slag. *J. Clean. Prod.* **2023**, *383*, 135439. [CrossRef]
11. Tian, K.; Wang, Y.; Dong, B.; Fang, G.; Xing, F. Engineering and micro-properties of alkali-activated slag pastes with Bayer red mud. *Constr. Build. Mater.* **2022**, *351*, 128869. [CrossRef]
12. Li, Z.; Gao, M.; Lei, Z.; Tong, L.; Sun, J.; Wang, Y.; Jiang, X. Ternary cementless composite based on red mud, ultra-fine fly ash, and GGBS: Synergistic utilization and geopolymerization mechanism. *Case Stud. Constr. Mater.* **2023**, *19*, e02410. [CrossRef]
13. Zhang, Y.; Liu, X.; Xu, Y.; Tang, B.; Wang, Y.; Mukiza, E. Synergic effects of electrolytic manganese residue-red mud-carbide slag on the road base strength and durability properties. *Constr. Build. Mater.* **2019**, *220*, 364–374. [CrossRef]
14. Wang, Y.; Liu, X.; Zhu, X.; Zhu, W.; Yue, J. Synergistic effect of red mud, desulfurized gypsum and fly ash in cementitious materials: Mechanical performances and microstructure. *Constr. Build. Mater.* **2023**, *404*, 133302. [CrossRef]
15. Zhang, J.; Li, S.; Li, Z. Investigation the synergistic effects in quaternary binder containing red mud, blast furnace slag, steel slag and flue gas desulfurization gypsum based on artificial neural networks. *J. Clean. Prod.* **2020**, *273*, 122972. [CrossRef]
16. Cui, W.; Liu, J.; Duan, W.; Xie, M.; Li, X.; Dong, X. Study on the synergistic effects and eco-friendly performance of red mud-based quaternary cementitious materials. *Constr. Build. Mater.* **2024**, *428*, 136352. [CrossRef]
17. Bai, Y.; Guo, W.; Wang, X.; Pan, H.; Zhao, Q.; Wang, D. Utilization of municipal solid waste incineration fly ash with red mud-carbide slag for eco-friendly geopolymer preparation. *J. Clean. Prod.* **2022**, *340*, 130820. [CrossRef]
18. Zhu, D.; Zhu, S.; Tang, A. Effect of clinoptilolite on properties and fractal characteristic of pore structure of polypropylene fiber-reinforced cement-based composite. *Constr. Build. Mater.* **2023**, *402*, 132964. [CrossRef]

19. Huo, W.; Zhu, Z.; Sun, H.; Gao, Q.; Zhang, J.; Wan, Y.; Zhang, C. Reaction kinetics, mechanical properties, and microstructure of nano-modified recycled concrete fine powder/slag based geopolymers. *J. Clean. Prod.* **2022**, *372*, 133715. [CrossRef]
20. Wang, L.; Jin, M.; Wu, Y.; Zhou, Y.; Tang, S. Hydration, shrinkage, pore structure and fractal dimension of silica fume modified low heat Portland cement-based materials. *Constr. Build. Mater.* **2021**, *272*, 121952. [CrossRef]
21. Han, X.; Wang, B.; Feng, J. Relationship between fractal feature and compressive strength of concrete based on MIP. *Constr. Build. Mater.* **2022**, *322*, 126504. [CrossRef]
22. Ren, Z.; Dong, W.; Dong, X. Analysis of fractal and erosion characteristics of aeolian sand concrete pore structure under capillary absorption. *J. Build. Eng.* **2025**, *104*, 112258. [CrossRef]
23. Zheng, D.; Song, W.; Fu, J.; Xue, G.; Li, J.; Cao, S. Research on mechanical characteristics, fractal dimension and internal structure of fiber reinforced concrete under uniaxial compression. *Constr. Build. Mater.* **2020**, *258*, 120351. [CrossRef]
24. Xue, G.; Fu, Q.; Xu, S.; Li, J. Macroscopic mechanical properties and microstructure characteristics of steel slag fine aggregate concrete. *J. Build. Eng.* **2022**, *56*, 104742. [CrossRef]
25. Han, X.; Feng, J.; Wang, B. Relationship between fractal feature and compressive strength of fly ash-cement composite cementitious materials. *Cem. Concr. Compos.* **2023**, *139*, 105052. [CrossRef]
26. Zhu, D.; Wen, A.; Mu, D.; Tang, A.; Jiang, L.; Yang, W. Investigation into compressive property, chloride ion permeability, and pore fractal characteristics of the cement mortar incorporated with zeolite powder. *Constr. Build. Mater.* **2024**, *411*, 134522. [CrossRef]
27. Zhang, P.; Ding, J.; Guo, J.; Wang, F. Fractal analysis of cement-based composite microstructure and its application in evaluation of macroscopic performance of cement-based composites: A review. *Fractal Fract.* **2024**, *8*, 304. [CrossRef]
28. Tian, G.; Deng, H.; Xiao, Y.; Yu, S. Experimental study of multi-angle effects of micron-silica fume on micro-pore structure and macroscopic mechanical properties of rock-like material based on NMR and SEM. *Materials* **2022**, *15*, 3388. [CrossRef]
29. Zhu, Z.; Huo, W.; Sun, H.; Ma, B.; Yang, L. Correlations between unconfined compressive strength, sorptivity and pore structures for geopolymer based on SEM and MIP measurements. *J. Build. Eng.* **2023**, *67*, 106011. [CrossRef]
30. *GB/T 18046*; Ground Granulated Blast Furnace Slag Used for Cement and Concrete. National Standards of the People's Republic of China: Beijing, China, 2017.
31. Yao, Y.; Wang, Y.; Wei, Q.; Cui, S.; Hao, L. Effect of the formation of amorphous networks on the structure and hydration characteristics of granulated blast furnace slag. *Materials* **2020**, *13*, 1462. [CrossRef]
32. Mudgal, M.; Singh, A.; Chouhan, R.K.; Acharya, A.; Srivastava, A.K. Fly ash red mud geopolymer with improved mechanical strength. *Clean. Eng. Technol.* **2021**, *4*, 100215. [CrossRef]
33. Liu, X.; Xiao, G.; Yang, D.; Dai, L.; Tang, A. Sustainable cementitious materials: Strength and microstructural characteristics of calcium carbide residue-activated ground granulated blast furnace slag–fly ash composites. *Sustainability* **2024**, *16*, 11168. [CrossRef]
34. Li, Z.; Dong, H.; Wang, Y.; Men, J.; Wang, J.; Zhao, X.; Zou, S. Valorization of alkali–thermal activated red mud for high-performance geopolymer: Performance evaluation and environmental effects. *Buildings* **2025**, *15*, 2471. [CrossRef]
35. Miricioiu, M.G.; Niculescu, V.C. Fly ash, from recycling to potential raw material for mesoporous silica synthesis. *Nanomaterials* **2020**, *10*, 474. [CrossRef]
36. *GB/T17671-2021*; Test Method of Cement Mortar Strength (ISO Method). Standards Press of China: Beijing, China, 2021.
37. Ye, H.; Radlińska, A. Fly ash-slag interaction during alkaline activation: Influence of activators on phase assemblage and microstructure formation. *Constr. Build. Mater.* **2016**, *122*, 594–606. [CrossRef]
38. Zhu, J.; Yue, H.; Ma, L.; Li, Z.; Bai, R. Study on hydration mechanism and environmental safety of thermal activated red mud-based cementitious materials. *Environ. Sci. Pollut. Res.* **2023**, *30*, 55905–55921. [CrossRef]
39. Tang, C.; Mu, X.; Ni, W.; Xu, D.; Li, K. Study on effects of refining slag on properties and hydration of cemented zsolid waste-based backfill. *Materials* **2022**, *15*, 8338. [CrossRef] [PubMed]
40. Yin, B.; Kang, T.; Kang, J.; Chen, Y. Analysis of active ion-leaching behavior and the reaction mechanism during alkali activation of low-calcium fly ash. *Int. J. Concr. Struct. Mater.* **2018**, *12*, 50. [CrossRef]
41. Kang, S.H.; Kang, H.; Lee, N.; Kwon, Y.H.; Moon, J. Development of cementless ultra-high performance fly ash composite (UHPFC) using nucleated pozzolanic reaction of low Ca fly ash. *Cem. Concr. Compos.* **2022**, *132*, 104650. [CrossRef]
42. Segawa, M.; Kurihara, R.; Aili, A.; Igarashi, G.; Maruyama, I. Shrinkage reduction mechanism of low Ca/Si ratio CASH in cement pastes containing fly ash. *Cem. Concr. Res.* **2024**, *186*, 107683. [CrossRef]
43. Han, F.; Zhu, Z.; Zhang, H.; Li, Y.; Fu, T. Effect of steel slag on the properties of alkali-activated slag material: A comparative study with fly ash. *Materials* **2024**, *17*, 2495. [CrossRef]
44. Huang, H.; Li, R.; Chen, F.; Cao, K.; Guo, L.; Qiu, Q. Mechanical Properties and Microscopic Fractal Characteristics of Lime-Treated Sandy Soil. *Fractal Fract.* **2025**, *9*, 64. [CrossRef]
45. Gao, Y.; Jing, H.W.; Yu, Z.X. Experimental study on the mechanical properties of crushed stone cemented by graphene oxide and cement-based composite grouting materials. *Chin. J. Rock Mech. Eng.* **2022**, *41*, 1898–1909.

46. Zhang, X.; Lv, Z.; Huang, H.; Li, R.; Qiu, Q.; Huang, Y. Evaluation of Mechanical Properties and Micro-Mechanism of Alkali-Activated Material with CG Under Ultrasonic Treatment from a Fractal Perspective. *Fractal Fract.* **2025**, *9*, 401. [CrossRef]
47. Li, Y.; Shen, A.; Wu, H. Fractal dimension of basalt fiber reinforced concrete (BFRC) and its correlations to pore structure, strength and shrinkage. *Materials* **2020**, *13*, 3238. [CrossRef]
48. Ding, K.; Zeng, C. Study on the compressive strength, pore structure characteristics, and fractal dimension of the ecological porous concrete specimens based on ordinary Portland cement. *Constr. Build. Mater.* **2025**, *483*, 141795. [CrossRef]
49. Jiang, Z.; Cai, G.; Liu, Y.; Wang, P.; Yu, S. Pore structure and mechanical characteristics of CRS mortar based on NMR and fractal theory. *Constr. Build. Mater.* **2024**, *457*, 139459. [CrossRef]
50. Zhang, P.; Han, X.; Guo, J.; Zhang, H. Fractal characteristics of geopolymer mortar containing municipal solid waste incineration fly ash and its correlations to pore structure and strength. *Fractal Fract.* **2022**, *6*, 676. [CrossRef]
51. Liu, Y.; Deng, H.; Jiang, Z.; Tian, G.; Wang, P.; Yu, S. Pore structure characteristics of artificial sand aggregate mortar. *J. Build. Eng.* **2024**, *94*, 109940. [CrossRef]
52. Song, B.; Li, Y.; Zhang, W. Effects of Harmless Municipal Solid Waste Incineration Fly Ash on the Macroscopic Properties and Microstructure of Recycled Aggregate Concrete. *Materials* **2025**, *18*, 1866. [CrossRef] [PubMed]
53. Wang, F.; Du, H.; Zheng, Z.; Xu, D.; Wang, Y.; Li, N.; Ren, C. The impact of fly ash on the properties of cementitious materials based on slag-steel slag-gypsum solid waste. *Materials* **2024**, *17*, 4696. [CrossRef] [PubMed]
54. Melichar, J.; Žižková, N.; Brožovský, J.; Mészárosová, L.; Hermann, R. Study of the interaction of cement-based materials for 3D printing with fly ash and superabsorbent polymers. *Buildings* **2022**, *12*, 2008. [CrossRef]
55. Wang, L.; Zeng, X.; Yang, H.; Lv, X.; Guo, F.; Shi, Y.; Hanif, A. Investigation and application of fractal theory in cement-based materials: A review. *Fractal Fract.* **2021**, *5*, 247. [CrossRef]

Disclaimer/Publisher's Note: The statements, opinions and data contained in all publications are solely those of the individual author(s) and contributor(s) and not of MDPI and/or the editor(s). MDPI and/or the editor(s) disclaim responsibility for any injury to people or property resulting from any ideas, methods, instructions or products referred to in the content.